THE JOURNAL OF PHYSICAL CHEMISTRY C

Article

pubs.acs.org/JPCC

The Effects of Mn^{2+} Precursors on the Structure and Ozone Decomposition Activity of Cryptomelane-Type Manganese Oxide (OMS-2) Catalysts

Caixia Wang,[†,‡] Jinzhu Ma,[*,†] Fudong Liu,[†,§] Hong He,[†] and Runduo Zhang[‡]

[†]State Key Joint Laboratory of Environment Simulation and Pollution Control, Research Center for Eco-Environmental Sciences, Chinese Academy of Sciences, Beijing 100085, China

[‡]State Key Laboratory of Chemical Resource Engineering, Beijing University of Chemical Technology, Beijing 100029, China

Supporting Information

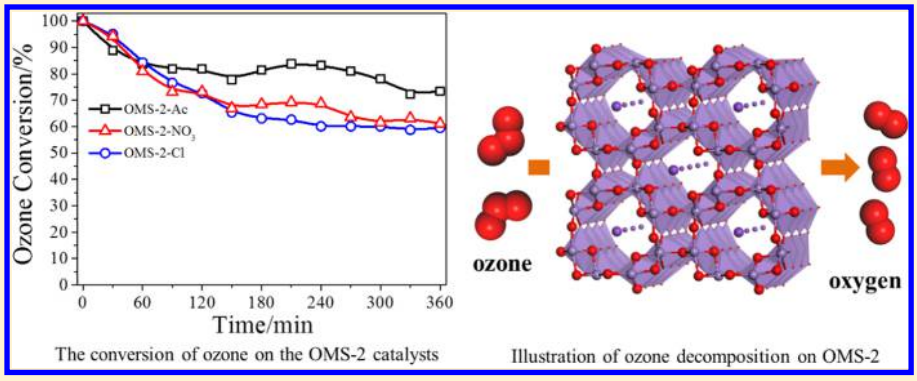

The conversion of ozone on the OMS-2 catalysts — Illustration of ozone decomposition on OMS-2

ABSTRACT: The effects of Mn^{2+} precursors on the structure and ozone decomposition activity of cryptomelane-type manganese oxide (OMS-2) catalysts were investigated under high-humidity conditions. The OMS-2 catalysts were synthesized using a hydrothermal approach. Characterization of OMS-2 was carried out using X-ray diffraction (XRD), scanning electron microscopy (SEM), N_2 physical adsorption, Raman spectroscopy, X-ray absorption fine structure (XAFS), H_2 temperature-programmed reduction (H_2-TPR), and inductively coupled plasma (ICP) spectroscopy. The OMS-2-Ac synthesized using $MnAc_2$ as a Mn^{2+} precursor showed the best catalytic activity for ozone decomposition (~80%) under RH = 90% and space velocity of 600000 h^{-1} and is a promising catalyst for purifying waste gases containing ozone under high-humidity conditions. Acetate groups could prevent the aggregation of manganese oxide particles, which may introduce more crystalline defects. On the basis of the characterization results, it is supposed that the greater surface area and higher amount of Mn^{3+} are the main factors that contribute to the excellent performance of OMS-2-Ac. This study can improve our understanding of ozone decomposition on OMS-2 catalysts and serve as a guide in using OMS-2 for ozone removal.

1. INTRODUCTION

As we all know, ozone is a double-edged sword. The ozone layer in the stratosphere can prevent ultraviolet light from reaching the earth directly and protect life on Earth. However, tropospheric ozone is a common pollutant that causes health problems to human beings including neurological disease, increased frequency of respiratory symptoms, and reduced immune system function.[1] Because of its powerful oxidizing ability, ozone is widely used in purification of wastewater and drinking water, oxidation of organic substances, and food preservation. The resulting tail gas still contains some amount of ozone, and its release into the environment must be avoided. The major indoor source of ground level ozone comes from photocopiers, laser printers, and other modern office equipment. Because most people spend a majority of time inside buildings, it is a significant cause of exposure. According to the U.S. Environmental Protection Agency (U.S. EPA) regulations, the allowable exposure to ozone in terms of 8 h average concentration is 0.075 ppm and the Chinese "indoor air quality standards" (GB/T 18883-2002) requires that the indoor ozone concentration should not exceed 0.07 ppm.[2] Therefore, the decomposition of ozone is an important area of research from the viewpoint of environmental protection and health.

Because it is safe, economical, and efficient, catalytic decomposition is the most effective method for purifying waste gases containing ozone. Metal oxide catalysts are reported to be among the most active catalysts for ozone decomposition, and considerable efforts have been directed toward the design of ozone decomposition catalysts based on noble metals (e.g., Pd, Au, and Ag)[3−6] or oxides of transition metals such as Mn,[7−9] Fe,[10−12] Cu,[13] Co,[14] and Ni.[15] Dhandapani and Oyama[16] pointed out that among the

Received: August 19, 2015
Revised: September 17, 2015
Published: September 18, 2015

DOI: 10.1021/acs.jpcc.5b08095
J. Phys. Chem. C 2015, 119, 23119−23126

common metal oxides (with γ-Al_2O_3 and cordierite as carrier), MnO_2 possessed the highest activity in the catalytic decomposition of ozone. Its better activity may be associated with its changeable valence and variety of morphologies. Manganese dioxides can exist in different crystal structures and morphologies.[17−26] Cryptomelane-type manganese oxide (OMS-2) is a form of manganese dioxide with a one-dimensional tunnel structure composed of 2 × 2 edge-shared MnO_6 octahedral chains, which are corner-connected to form 4.6 × 4.6 Å tunnels.[27−31] Manganese is present in OMS-2 as Mn^{2+}, Mn^{3+}, and Mn^{4+} located in octahedral sides, and potassium ions reside in the tunnels along with a small amount of water to stabilize the tunnel structure.[32−35] The mechanism of ozone catalytic decomposition consists mainly of redox steps, thus the presence of mixed-valent manganese ions probably accelerates the ozone decomposition. The redox pair of Mn(IV)/Mn(III) in OMS-2 seems to facilitate the oxidation process.[33,36] Peluso et al.[37] also pointed out that a high concentration of Mn^{3+} in the OMS-2 framework could result in weak Mn−O bonds and form more active oxygen species. Luo et al.[38] reported that OMS-2 prepared using a refluxing method in buffer solution possessed excellent hydrophobicity, which could enable it to resist water and slow down the loss of activity of the catalysts. From the above discussion, it can be seen that the properties of OMS-2 as a catalyst, such as the large surface area, mixed valence manganese species and excellent hydrophobicity, could be predicted to promote the catalytic decomposition of ozone. However, to the best of our knowledge, the use of OMS-2 materials for ozone decomposition has not been reported.

OMS-2 materials are usually prepared via reaction between Mn^{2+} and potassium permanganate with a hydrothermal method. Different Mn^{2+} precursors can have varying effects on the properties of OMS-2, such as crystallinity, surface area, and redox properties and consequently affect the catalytic performance.[27] In this work, OMS-2 catalysts were successfully prepared by using different Mn^{2+} precursors. The as-prepared OMS-2 catalysts were characterized by XRD, SEM, N_2 adsorption−desorption, Raman, XAFS, H_2-TPR, and ICP. The catalytic performance was systematically evaluated by decomposition of ozone under high relative humidity.

2. EXPERIMENTAL SECTION

2.1. Catalyst Synthesis. The OMS-2 materials were prepared via reaction between Mn^{2+} and potassium permanganate with a hydrothermal method, which involved a variation of the procedure used by Luo et al.[39] A typical procedure was as follows: 3.668 g of $MnAc_2{\cdot}4H_2O$ was dissolved in 35 mL deionized water under stirring. 2.5 mL Glacial acetic acid was then added in order to form an acidic environment. Next, a solution of 2.168 g $KMnO_4$ in 40 mL deionized water was added to the above mixture under stirring. Finally, the mixed solution was maintained at 100 °C for 24 h in a Teflon-lined autoclave and then cooled to room temperature. The resulting black slurry was centrifuged, washed by deionized water, and dried at 100 °C in an oven overnight for characterization and catalytic evaluation. The OMS-2 material obtained by this way was called OMS-2-Ac. For comparison, two other catalysts, OMS-2-NO_3 and OMS-2-Cl, were synthesized by the same method with manganese nitrate [$Mn(NO_3)_2$] and manganese chloride ($MnCl_2{\cdot}4H_2O$) as Mn^{2+} precursors, respectively. Amorphous MnO_2 was prepared with the method used by Mizuno.[40] First an aqueous solution of $KMnO_4$ (2.168g, 40 mL) was added dropwise to an aqueous solution of $MnAc_2{\cdot}4H_2O$ (3.668 g) and HAc (2.5 mL). The resulting mixture was stirred at room temperature for 30 min. Then, the dark brown solid formed was filtered off, washed with a large amount of deionized water, and dried under air at 100 °C overnight. The amorphous structure of the as-prepared material was confirmed by XRD (Figure S1).

2.2. Catalyst Characterization. The crystalline structure of the catalysts was determined by a powder X-ray diffractometer (XRD; X'Pert PRO, PANalytical) using Cu Kα (λ = 0.154 06 nm) radiation at 40 kV and 40 mA. The data of 2θ from 5 to 80° were collected with the step size of 0.065°.

The morphologies of the OMS-2 materials were investigated using a SU8000 field emission scanning electron microscope (FESEM), and the accelerating voltage was 3000 V. The samples for FESEM measurements were prepared by depositing the powder on a conductive tape using N_2 vertical purging.

The surface area and pore structure (volume and size) of the catalysts were determined with a physisorption analyzer (Autosorb-1C-TCD, Quantachrome) by N_2 adsorption−desorption at 77 K. Prior to the N_2 physisorption, all samples were degassed at 90 °C for 12 h to evacuate the physisorbed moisture before measurement. The surface area (S_{BET}) was determined by applying the Brunauer−Emmett−Teller (BET) method to the adsorption isotherm in the partial pressure range of 0.05−0.35. The pore volume (V_{BJH}) and the pore diameter (D_{BJH}) were determined by the Barrett−Joyner−Halenda (BJH) equation from the desorption isotherm.

Raman spectra of the catalysts were recorded at room temperature on a homemade UV resonance Raman spectrometer (UVRDLPC-DL-03), which consisted of three optional excitation lasers (244, 325, and 532 nm), a three-stage grating spectrograph, and a CCD detector cooled by liquid nitrogen. The instrument was calibrated against the Stokes Raman signal of Teflon at 1378 cm^{-1}. A continuous diode-pumped solid state (DPSS) laser beam (532 nm) was used as the exciting radiation, and the power output was about 48 mW. The diameter of the laser spot on the sample surface was focused at 25 μm. The spectral resolution was 2.0 cm^{-1}. All Raman spectra used in the paper were original and unsmoothed.

The X-ray absorption near edge structure (XANES) and extended X-ray absorption fine structure (EXAFS) of the Mn−K edge in the OMS-2 catalysts were measured in transmission mode at room temperature on the 1W1B beamline, Beijing Synchrotron Radiation Facility and BL14W1 beamline, Shanghai Synchrotron Radiation Facility. Data processing was performed by the software IFeffit1.2.11. XANES data were normalized with edge height and then the first-order derivatives were taken to compare the variation of absorption edge energies. EXAFS oscillation $\chi(k)$ was extracted using spline smoothing with a Cook-Sayers criterion, and the filtered k^3-weighted $\chi(k)$ was Fourier transformed into R space in the k range of 3−12 $Å^{-1}$. In the curve-fitting step, the possible backscattering amplitude and phase shift were calculated using FEFF8.4 code.

The H_2 temperature-programmed reduction (H_2-TPR) measurements were carried out using a Micromeritics AutoChem 2920 chemisorption analyzer equipped with a TCD detector. About 50 mg of sample was loaded in a U-shaped quartz reactor and pretreated at 100 °C in a flow of air (50 mL/min) for 1 h. After cooling the reactor to room

DOI: 10.1021/acs.jpcc.5b08095
J. Phys. Chem. C 2015, 119, 23119−23126

temperature, the catalyst was then heated to 1000 °C in a 10 vol % H_2/Ar gas flow of 50 mL/min at a heating rate of 10 °C/min.

The mass ratio K/Mn of the catalysts was analyzed using an inductively coupled plasma instrument (OPTIMA 8300) with a radial view of the plasma. All samples were dissolved using strong acid solution before tested. The calibration solution was prepared using pure materials. The average of three atomic emission lines was used to determine the mass ratio K/Mn in the catalysts.

2.3. Catalyst Activity for Ozone Decomposition. The catalytic performance for ozone decomposition was tested in a fixed bed continuous flow quartz reactor (4 mm i.d.) at a temperature of 30 °C and a space velocity of 600000 h^{-1}. The total gas flow was 1000 mL/min with 800 mL/min N_2 and 200 mL/min O_2. Ozone was generated by low-pressure ultraviolet lamps (185 nm, Beijing Lighting Research Institute) and the inlet ozone concentration was 40 ± 2 ppm. Inlet and outlet ozone concentrations were analyzed by an ozone monitor (model 202, 2B Technologies). The temperature and pressure drop were also recorded at the same time to verify uniformity throughout the experiments. Ozone conversion was calculated on the basis of the following equation:

$$O_3 \text{ conversion} = \frac{C_{in} - C_{out}}{C_{in}} \times 100\%$$

3. RESULTS AND DISCUSSION

Figure 1 shows the ozone decomposition activity over the OMS-2 catalysts and amorphous MnO_2 material when relative humidity (RH) was 45%. The activities of OMS-2-Ac and OMS-2-NO_3 were nearly 100% even after 6 h. The activity of OMS-2-Cl decreased with time, to only 85% after 6 h. However, the amorphous MnO_2 material was by far the least active, with a conversion percentage of only 35% after 6 h. The OMS-2 catalysts showed high activity for ozone decomposition compared with nonporous manganese oxides, which may be due to the special structure of the OMS-2 material.

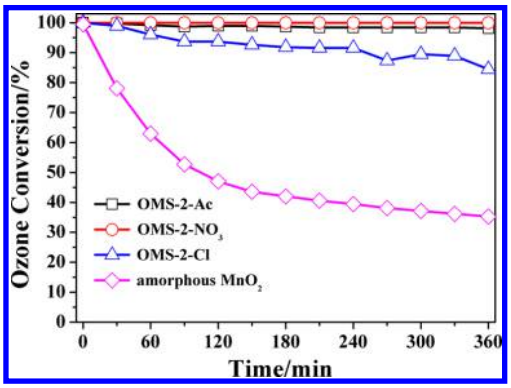

Figure 1. Conversion of ozone on the OMS-2 catalysts and amorphous MnO_2 material at RH = 45%.

Water vapor has a severe influence on catalytic performance in ozone decomposition. H_2O molecules compete with ozone for adsorption, leading to a decrease in catalytic activity.[41] When the RH was 90%, ozone conversion over these catalysts decreased to greater or lesser extents (Figure 2). Compared with the other catalysts, OMS-2-Ac maintained better ozone conversion performance (~75%), which indicates that the OMS-2-Ac catalyst has good hydrophobicity. It also can be seen that the activity decreased during the first 2 h and then stabilized. Initially, the H_2O molecules may compete with ozone for adsorption, and the activity decreased. However, the effect of high RH on the active sites and the cryptomelane structure needs further research.

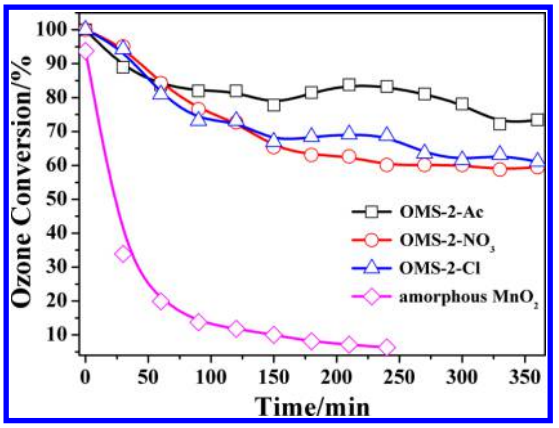

Figure 2. Conversion of ozone on the OMS-2 catalysts and amorphous MnO_2 material at RH = 90%.

The XRD patterns of the as-prepared catalysts derived from different Mn^{2+} precursors are depicted in Figure 3. The catalysts prepared from the different precursors were well-crystallized with the cryptomelane structure, characteristic of the octahedral molecular sieve material OMS-2 (JCPDS 29-1020). The variations in peak broadening among the synthesized materials revealed differences in crystal size. The sizes of OMS-2 crystals prepared with different precursors were calculated from the line broadening of XRD peaks using Scherrer's formula ($d = 0.9\lambda/\beta \cos \theta$). The as-calculated crystal sizes of OMS-2-Ac, OMS-2-NO_3, and OMS-2-Cl were 9.0, 11.4, and 12.1 nm, respectively.

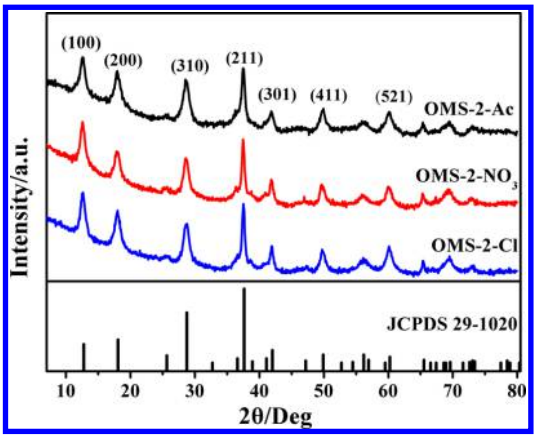

Figure 3. XRD patterns of the OMS-2 catalysts.

Figure 4 shows the FESEM images of the samples obtained from different precursors. All of the samples displayed fibrous morphologies typical of cryptomelane, regardless of the precursors used. On the basis of measurements of 100 particles for each catalyst material, the average diameters of OMS-2-Ac, OMS-2-NO_3, and OMS-2-Cl were 8.9 ± 2.0, 11.9 ± 2.1, and 14.1 ± 2.4 nm, respectively. This was consistent with the XRD results.

DOI: 10.1021/acs.jpcc.5b08095
J. Phys. Chem. C 2015, 119, 23119−23126

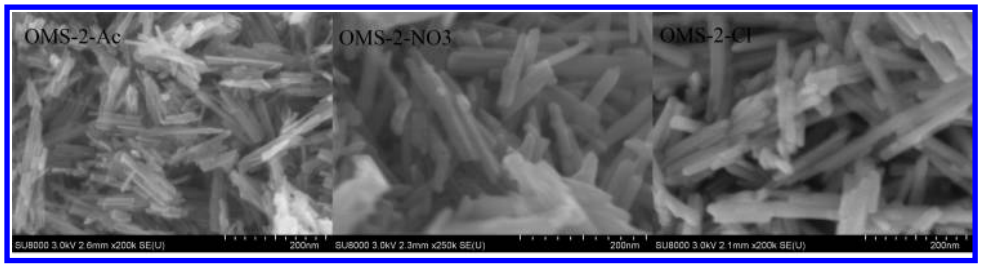

Figure 4. FESEM images of the OMS-2 catalysts.

The OMS-2-Ac catalyst showed the smallest particle diameter, consistent with the results calculated from the XRD peaks. Combining the results obtained from XRD and FESEM, it can be speculated that the $MnAc_2$ precursor resulted in the formation of a smaller particle diameter for the OMS-2-Ac catalyst, which is probably related to the presence of acetate groups in the solution. When using $MnAc_2$ as the precursor, the concentration of acetate groups in solution was 0.5 mol/L, much higher than that in the solutions for the other two precursors (0.006 mol/L). Carbonyl groups from the acetate in the solution and the surface OH groups on the manganese oxide materials may have formed bonds, which could cause the isolation of manganese oxide particles from each other by the surrounding acetate groups and prevent further aggregation.[42]

Smaller particles can introduce more defects and enhance the surface area. The N_2 adsorption−desorption isotherms of the three OMS-2 catalysts are shown in Figure 5. All of the samples

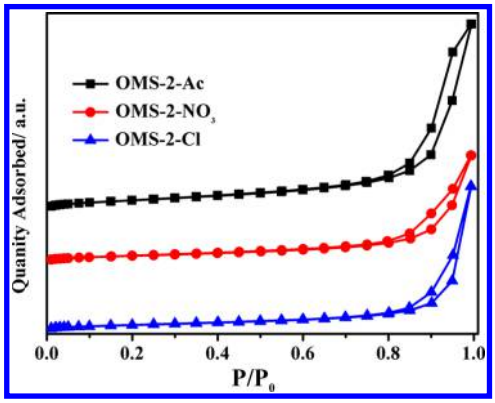

Figure 5. N_2 adsorption−desorption isotherms of the OMS-2 catalysts.

show similar N_2 adsorption/desorption isotherms typical of mesoporous materials. The isotherms show a characteristic type II isotherm pattern for the three catalysts, with microporous filling at low P/P_0 and capillary condensation at high P/P_0. The surface areas of OMS-2-Ac, OMS-2-NO_3, and OMS-2-Cl were 137, 83, and 78 m^2/g, respectively. Large surface area can provide more sites for the adsorption of ozone and thus improve the catalytic performance for ozone decomposition on OMS-2-Ac.

Compared with XRD, Raman spectroscopy is more surface-sensitive for the characterization of the catalysts. Figure 6 shows the Raman spectra of the OMS-2 catalysts. All the synthesized OMS-2 materials showed bands at 180, 386, 506, 576, and 630 cm^{-1}. The first three bands correspond to the deformation modes of the metal−oxygen chain of Mn−O−Mn, and the distinct bands at 576 and 630 cm^{-1} correspond to the stretching mode of the Mn−O lattice.[27,43−45] The OMS-2-Ac

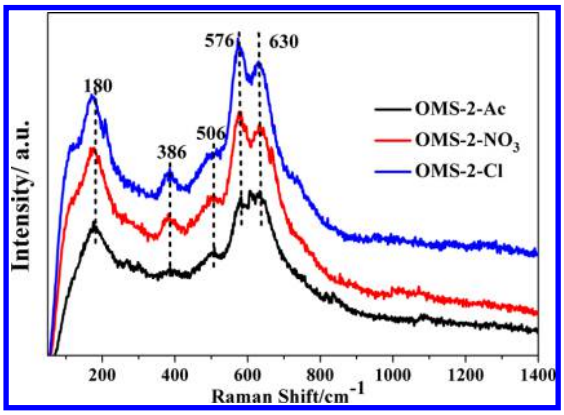

Figure 6. Raman spectra of the OMS-2 catalysts.

catalyst showed Raman spectra characteristics similar to both OMS-2-NO_3 and OMS-2-Cl but gave much broader and weaker peaks. This is a size-dependent phenomenon commonly observed with nanoparticles and can be explained by the inhomogeneous strain broadening associated with dispersion in particle size and by phonon confinement.[46] This observation is consistent with the XRD and SEM measurements, in which the particle diameter of the OMS-2 samples decreases in the sequence of OMS-2-Cl > OMS-2-NO_3 > OMS-2-Ac.

X-ray absorption fine structure (XAFS), including X-ray absorption near edge structure (XANES) and extended X-ray absorption fine structure (EXAFS), was used to determine the electronic and structural properties of the catalysts. The EXAFS study of MnO_2 is fairly straightforward since it has only one kind of Mn site. The XAFS of the Mn−K edge, including XANES and EXAFS, were measured using Mn foil, MnO, Mn_2O_3, and MnO_2 as reference samples. The full XAFS spectra of all the catalysts are listed in Figure S2. As shown in Figure 7A, the XANES spectra of MnO_2 and Mn_2O_3 were similar, and both the pre-edge peaks and the postedge regions of Mn−K XANES in OMS-2 catalysts were similar to those spectra. Yet, no obvious differences between the catalysts prepared by different precursors were observed. Afterward, to further determine the average valence of Mn species in our catalysts, the first-order derivatives of Mn−K XANES in the series of MnO_x catalysts were taken and compared with those in the reference samples.[47] As shown in Figure 7B, the Mn K-edge absorption energy (E_0) of the reference materials was determined to be 6548.4 and 6552.8 eV for Mn_2O_3 and MnO_2. The absorption edge energy of Mn species in MnO_x catalysts was 6551.8 eV, which was slightly less than that in MnO_2, most probably due to the presence of a small amount of Mn^{3+}. The exact amount of Mn^{3+} in OMS-2 catalysts calculated by the Rex2000 analysis package was 14.4%, 3.12%, and 2.12% for OMS-2-Ac, OMS-2-NO_3, and OMS-2-Cl, respectively. Linear combination fitting of the XANES spectra of the

DOI: 10.1021/acs.jpcc.5b08095
J. Phys. Chem. C 2015, 119, 23119−23126

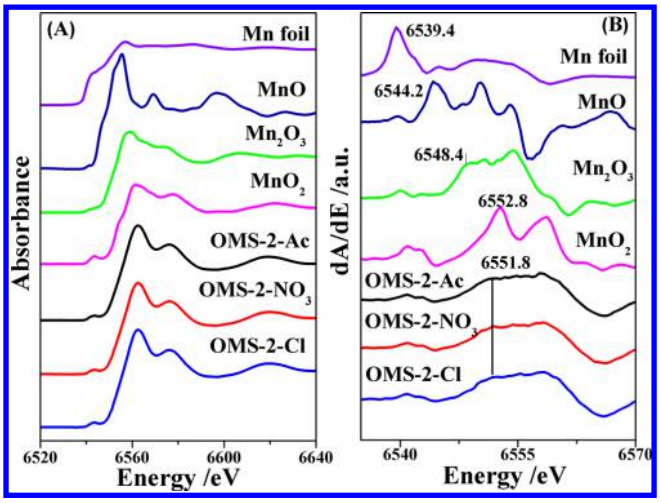

Figure 7. (A) XANES and (B) first-order derivatives of XANES of the Mn−K edge in series of MnOx catalysts and Mn-containing reference samples.

OMS-2 catalysts with Mn foil, MnO, Mn_2O_3, and MnO_2 reference materials showed that the percentage of Mn_2O_3 in the catalysts was 7.2, 1.5, and 1%, respectively. These results indicate that the electronic and local structure of our MnO_x catalysts is similar to that of MnO_2, which is in good accordance with the XRD results.

Figure 8A shows the filtered k^3-weighted EXAFS oscillations Fourier transformed into R space of the Mn−K edge in the series of OMS-2 catalysts, and Figure 8B shows the corresponding filtered $k^3 \cdot \chi(k)$ in the k range of 3−12 Å^{-1}. It should be noted that the EXAFS of the OMS-2 catalysts was modeled based on the structure of MnO_2, and no contribution from Mn_2O_3 was considered in the fitting of these catalysts. Because the highest proportion of MnO_x in the form of Mn_2O_3 in our three OMS-2 materials is only 7.2%, this fitting is reasonable.[48] The single and multiple scattering paths from the tetragonal cryptomelane structure (space group $I4/m$) of α-MnO_2 were used as the reference model. The crystal structure of the reference material is listed in Table S1. As also shown in Figure 8A, due to the residual potassium species in the catalysts, the coordination shells of Mn−O and Mn−Mn in our catalysts were different to a certain extent when compared with those in the MnO_2 standard samples (e.g., the relative peak intensity of Mn−Mn_1 and Mn−Mn_2). These potassium ions occupied the interstitial sites formed by the stacking of Mn−O octahedrons.[49] From Figure 8B, we can see that good curve fitting degrees could be obtained between experimental data and theoretical results, and the curve fitted data are presented in Table 2.

Table 2. Curve-Fitting Results of Mn K-Edge EXAFS in OMS-2 Catalysts Prepared Using Different Precursors

sample	Mn−K reference	shell	CN[a]	R[b] (Å)	DW[c] (Å)	R factor (%)
MnO_2	α-MnO_2	Mn−O	5.9	1.91	0.063	0.3
		Mn−Mn_1	4.0	2.86	0.082	
		Mn−Mn_2	4.0	3.44	0.032	
OMS-2-Ac	α-MnO_2	Mn−O	5.6	1.92	0.06	2
		Mn−Mn_1	4.0	2.87	0.057	
		Mn−Mn_2	2.6	3.4	0.05	
OMS-2-NO_3	α-MnO_2	Mn−O	6.2	1.92	0.057	0.8
		Mn−Mn_1	4.2	2.86	0.06	
		Mn−Mn_2	3.5	3.43	0.06	
OMS-2-Cl	α-MnO_2	Mn−O	6.0	1.92	0.041	0.8
		Mn−Mn_1	4.2	2.86	0.058	
		Mn−Mn_2	3.5	3.41	0.066	

[a]CN: coordination number. [b]R: bond distance. [c]DW: Debye−Waller factor.

After curve fitting, the reference material (α-MnO_2) was confirmed to possess Mn−O, Mn−Mn_1, and Mn−Mn_2 coordination shells at ca. 1.91, 2.86, and 3.44 Å with the coordination numbers being 5.9, 4.0, and 4.0, respectively. Moreover, it is clear that not only the first coordination shell of Mn−O but also the second coordination shells of Mn−Mn_1 plus Mn−Mn_2 in OMS-2 samples prepared from manganese nitrate and manganese chloride are almost the same as those in the MnO_2 reference sample.

However, the OMS-2-Ac catalyst prepared from manganese acetate showed a relatively small coordination number for the Mn−Mn_2 coordination shell and had the best ozone decomposition performance, suggesting that this catalyst possessed the most abundant surface defects,[50] which was

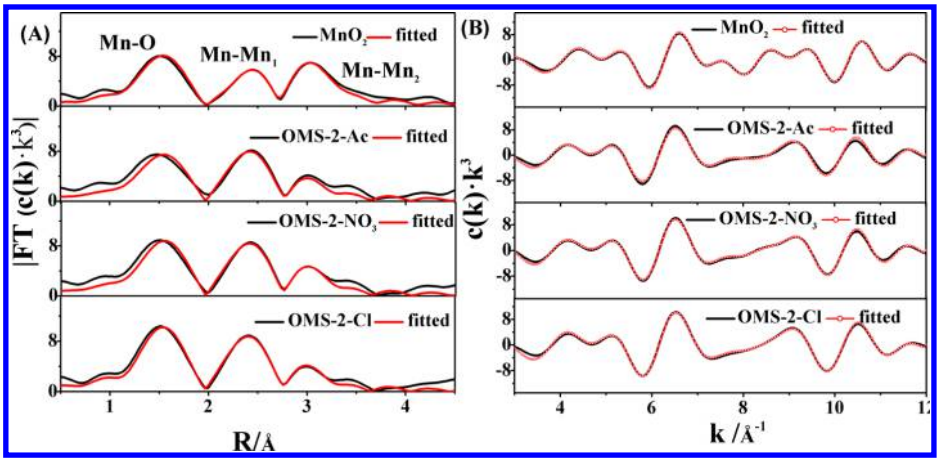

Figure 8. EXAFS spectra of Mn K-edge in series of MnOx catalysts: (A) Fourier transforms of filtered $k^3 \times \chi(k)$ into R space, where the red-dashed lines correspond to the curve-fitting results and (B) filtered $k^3 \times \chi(k)$ in the k range of 3−12 Å^{-1}, where the red-dotted lines correspond to the curve-fitting results.

DOI: 10.1021/acs.jpcc.5b08095
J. Phys. Chem. C 2015, 119, 23119−23126

beneficial to the adsorption and activation of ozone. The Mn−Mn_2 species, with longer bond length than that of Mn−Mn_1 species, might be the real active center in our reaction.

Temperature-programmed reduction is an important characterization technique to study the redox properties of metal oxide catalysts. The H_2-TPR profiles obtained for the OMS-2 catalysts are presented in Figure 9. It could be observed that

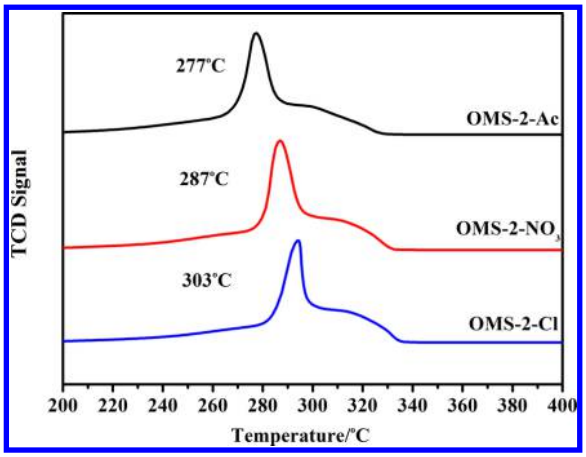

Figure 9. TPR profiles of the OMS-2 catalysts.

OMS-2 prepared from different precursors all showed two overlapped reduction peaks, which corresponded to a two-step reduction process. The reduction characteristics of materials with the cryptomelane structure have been described elsewhere. The lower temperature reduction process could be assigned to the MnO_2 to Mn_3O_4 reduction and that at high temperature to the further reduction to MnO.[51,52] Nevertheless, the number and intensity of the peaks on the TPR profiles can also depend on the different local environments of such species. In accordance with the literature, the mechanism of ozone decomposition consists mainly of redox steps: adsorption of ozone on the catalysts and desorption of the adsorbed intermediates.[53] Consequently, the faster the catalyst undergoes reduction, the faster will be the rate of the decomposition reaction. As shown in Figure 9, the OMS-2-Ac catalyst, with the best ozone decomposition activity, had the lowest reduction temperature, which is in good accordance with the results obtained by Oyama et al.[16]

By assuming Mn^{2+} as the final oxidation state, the average oxidation state (AOS) was calculated for Mn in the catalysts (according to its hydrogen consumption) and listed in Table 3. A lower AOS implies a higher fraction of Mn^{3+} in the catalyst. The fraction of Mn^{3+} was calculated to be 16%, 3%, and 2% for OMS-2-Ac, OMS-2-NO_3, and OMS-2-Cl, respectively, which was consistent with the values calculated by XANES (Table 3). The K/Mn mass ratio of the OMS-2 catalysts determined by ICP was also given in Table 3. K^+ ions are situated into the channels of the OMS-2 structure in order to stabilize it by providing charge balance, so a higher K/Mn ratio means a lower manganese oxidation state, which is consistent with the results of XANES and H_2-TPR. DFT calculations have confirmed that the presence of K^+ located in the tunnels of OMS-2 can improve its lattice oxygen activity, and the higher the concentration of K^+, the lower the removal energy of lattice oxygen.[32] In this study, the concentration of K^+ is higher in OMS-2-AC, thus the removal energy of lattice oxygen is lower, which is beneficial for the ozone decomposition.

Table 3. ICP, XANES, and H_2-TPR Values of the OMS-2 Catalysts

	ICP	XANES	H_2-TPR		
catalysts	K/Mn (%)	Mn^{3+} (%)	H_2 consumption (mmol/g)	AOS	Mn^{3+} (%)
OMS-2-Ac	8.274	14.4	11.01	3.84	16
OMS-2-NO_3	7.406	3.12	11.76	3.97	3
OMS-2-Cl	7.476	2.12	11.75	3.98	2

The mixed valency in OMS-2 catalysts was important for electron transport because the efficiencies of catalysts, especially those serving as catalysts for redox reactions, are usually governed by their ability and tendency to cycle between different valence states of the relevant cationic ions.[54] Ozone decomposition on the surface of OMS-2 could be presented by the following reaction scheme:

$$O_3 + [Mn^{3+}] \rightarrow O_2 + O^-_{ads}[Mn^{4+}]$$

$$O_3 + O^-_{ads}[Mn^{4+}] \rightarrow 2O_2 + [Mn^{3+}]$$

Abundant Mn^{3+} present on the surface of the catalyst could favor the ozone decomposition. A linear correlation between ozone decomposition and Mn^{3+} content (wt %) was found by Liu et al. on AgMn/HZSM-5.[55] Therefore, the higher content of Mn^{3+} also contributed to the high decomposition of ozone on OMS-2-AC.

4. CONCLUSIONS

The effects of different Mn^{2+} precursors on the structure and ozone decomposition activity of OMS-2 catalysts were investigated under high-humidity conditions. The OMS-2-Ac material prepared using $MnAc_2$ as the Mn^{2+} precursor displayed higher ozone conversion and better hydrophobicity than catalysts prepared using $Mn(NO_3)_2$ or $MnCl_2$. Under gas hour space velocity (GHSV) of 600000 h^{-1} and relative humidity of 90%, the OMS-2-Ac catalyst maintained almost 80% conversion after 6 h, which is promising for the purification of waste gases containing ozone under high-humidity conditions. Compared with the other two Mn^{2+} precursors, acetate groups could prevent the aggregation of manganese oxide and form smaller particles as well as abundant Mn^{3+}. The OMS-2-Ac catalyst tended to expose more defects due to its smaller particles and lower Mn−Mn coordination numbers. OMS-2-AC has a greater surface area and also contains the highest amount of Mn^{3+} species, therefore, presenting the highest activity of the three types of OMS-2 catalyst. This study can improve our understanding of ozone decomposition on OMS-2 catalysts and serve as a guide in using OMS-2 for ozone removal.

■ ASSOCIATED CONTENT

Supporting Information

The Supporting Information is available free of charge on the ACS Publications website at DOI: 10.1021/acs.jpcc.5b08095.

XRD patterns of the amorphous MnO_2 material, XAFS spectra of the OMS-2 catalysts, and crystal structure of the reference material (PDF)

DOI: 10.1021/acs.jpcc.5b08095
J. Phys. Chem. C 2015, 119, 23119−23126

AUTHOR INFORMATION

Corresponding Author

*E-mail: jzma@rcees.ac.cn.

Present Address

§Materials Sciences Division, Lawrence Berkeley National Laboratory, 1 Cyclotron Road, Berkeley, CA 94720, United States.

Notes

The authors declare no competing financial interest.

ACKNOWLEDGMENTS

This work was supported by the Strategic Priority Research Program of the Chinese Academy of Sciences (Grant XDB05050600) and the National Natural Science Foundation of China (Grants 21207145 and 51221892).

REFERENCES

(1) Levy, J. I.; Carrothers, T. J.; Tuomisto, J. T.; Hammitt, J. K.; Evans, J. S. Assessing the Public Health Benefits of Reduced Ozone Concentrations. *Environ. Health Perspect.* **2001**, *109*, 9−20.

(2) Rakitskaya, T. L.; Bandurko, A. Y.; Ennan, A. A.; Paina, V. Y.; Rakitskiy, A. S. Carbon-Fibrous-Material-Supported Base Catalysts of Ozone Decomposition. *Microporous Mesoporous Mater.* **2001**, *43*, 153−160.

(3) Yu, Q. W.; Pan, H.; Zhao, M.; Liu, Z. M.; Wang, J. L.; Chen, Y. Q.; Gong, M. C. Influence of Calcination Temperature on the Performance of Pd-Mn/Sio_2-Al_2o_3 Catalysts for Ozone Decomposition. *J. Hazard. Mater.* **2009**, *172*, 631−634.

(4) Zhang, P. Y.; Zhang, B.; Shi, R. Catalytic Decomposition of Low Level Ozone with Gold Nanoparticles Supported on Activated Carbon. *Front. Environ. Sci. Eng. China* **2009**, *3*, 281−288.

(5) Naydenov, A.; Konova, P.; Nikolov, P.; Klingstedt, F.; Kumar, N.; Kovacheva, D.; Stefanov, P.; Stoyanova, R.; Mehandjiev, D. Decomposition of Ozone on Ag/Sio_2 Catalyst for Abatement of Waste Gases Emissions. *Catal. Today* **2008**, *137*, 471−474.

(6) Ren, C. J.; Zhou, L. N.; Shang, H. Y.; Chen, Y. Q. Pd-Mnox/Γ-Al_2o_3 Monolithic Catalysts Prepared by Impregnation Method and Effect of Different Supports on Ground-Level Ozone Decomposition. *Acta Phys. Chim. Sin.* **2014**, *30*, 957−964.

(7) Einaga, H.; Futamura, S. Catalytic Oxidation of Benzene with Ozone over Alumina-Supported Manganese Oxides. *J. Catal.* **2004**, *227*, 304−312.

(8) Jiang, C. J.; Zhang, P. Y.; Zhang, B.; Li, J. G.; Wang, M. X. Facile Synthesis of Activated Carbon-Supported Porous Manganese Oxide Via in Situ Reduction of Permanganate for Ozone Decomposition. *Ozone: Sci. Eng.* **2013**, *35*, 308−315.

(9) Sui, M. H.; Liu, J.; Sheng, L. Mesoporous Material Supported Manganese Oxides (Mnox/Mcm-41) Catalytic Ozonation of Nitrobenzene in Water. *Appl. Catal., B* **2011**, *106*, 195−203.

(10) Heisig, C.; Zhang, W. M.; Oyama, S. T. Decomposition of Ozone Using Carbon-Supported Metal Oxide Catalysts. *Appl. Catal., B* **1997**, *14*, 117−129.

(11) Mehandjiev, D.; Naidenov, A. Ozone Decomposition on A-Fe_2o_3 Catalyst. *Ozone: Sci. Eng.* **1992**, *14*, 277−282.

(12) Lian, Z. H.; Ma, J. Z.; He, H. Decomposition of High-Level Ozone under High Humidity over Mn−Fe Catalyst: The Influence of Iron Precursors. *Catal. Commun.* **2015**, *59*, 156−160.

(13) Spasova, I.; Nikolov, P.; Mehandjiev, D. Ozone Decomposition over Alumina-Supported Copper, Manganese and Copper-Manganese Catalysts. *Ozone: Sci. Eng.* **2007**, *29*, 41−45.

(14) Tang, W. X.; Liu, H. D.; Wu, X. F.; Chen, Y. F. Higher Oxidation State Responsible for Ozone Decomposition at Room Temperature over Manganese and Cobalt Oxides: Effect of Calcination Temperature. *Ozone: Sci. Eng.* **2014**, *36*, 502−512.

(15) Mehandjiev, D.; Naydenov, A.; Ivanov, G. Ozone Decomposition, Benzene and Co Oxidation over $Nimno_3$-Ilmenite and $Nimn_2o_4$-Spinel Catalysts. *Appl. Catal., A* **2001**, *206*, 13−18.

(16) Dhandapani, B.; Oyama, S. T. Gas Phase Ozone Decomposition Catalysts. *Appl. Catal., B* **1997**, *11*, 129−166.

(17) Chen, T.; Dou, H. Y.; Li, X. L.; Tang, X. F.; Li, J. H.; Hao, J. M. Tunnel Structure Effect of Manganese Oxides in Complete Oxidation of Formaldehyde. *Microporous Mesoporous Mater.* **2009**, *122*, 270−274.

(18) Bai, B. Y.; Li, J. H.; Hao, J. M. 1d-Mno_2, 2d-Mno_2 and 3d-Mno_2 for Low-Temperature Oxidation of Ethanol. *Appl. Catal., B* **2015**, *164*, 241−250.

(19) Wang, F.; Dai, H. X.; Deng, J. G.; Bai, G. M.; Ji, K. M.; Liu, Y. X. Manganese Oxides with Rod-, Wire-, Tube-, and Flower-Like Morphologies: Highly Effective Catalysts for the Removal of Toluene. *Environ. Sci. Technol.* **2012**, *46*, 4034−4041.

(20) Wasalathanthri, N. D.; Poyraz, A. S.; Biswas, S.; Meng, Y.; Kuo, C.-H.; Kriz, D. A.; Suib, S. L. High-Performance Catalytic Ch_4 Oxidation at Low Temperatures: Inverse Micelle Synthesis of Amorphous Mesoporous Manganese Oxides and Mild Transformation to $K_{2-x}mn_8o_{16}$ and ϵ-Mno_2. *J. Phys. Chem. C* **2015**, *119*, 1473−1482.

(21) Li, D. Y.; Wu, X. F.; Chen, Y. F. Synthesis of Hierarchical Hollow Mno_2 Microspheres and Potential Application in Abatement of Vocs. *J. Phys. Chem. C* **2013**, *117*, 11040−11046.

(22) Zhang, J.; Li, Y.; Wang, L.; Zhang, C.; He, H. Catalytic Oxidation of Formaldehyde over Manganese Oxides with Different Crystal Structures. *Catal. Sci. Technol.* **2015**, *5*, 2305−2313.

(23) Chen, H.; He, J.; Zhang, C.; He, H. Self-Assembly of Novel Mesoporous Manganese Oxide Nanostructures and Their Application in Oxidative Decomposition of Formaldehyde. *J. Phys. Chem. C* **2007**, *111*, 18033−18038.

(24) Gao, T.; Glerup, M.; Krumeich, F.; Nesper, R.; Fjellvåg, H.; Norby, P. Microstructures and Spectroscopic Properties of Cryptomelane-Type Manganese Dioxide Nanofibers. *J. Phys. Chem. C* **2008**, *112*, 13134−13140.

(25) Tang, C.-L.; Wei, X.; Jiang, Y.-M.; Wu, X.-Y.; Han, L. N.; Wang, K.-X.; Chen, J.-S. Cobalt-Doped Mno2 Hierarchical Yolk−Shell Spheres with Improved Supercapacitive Performance. *J. Phys. Chem. C* **2015**, *119*, 8465−8471.

(26) Durand, J. P.; Senanayake, S. D.; Suib, S. L.; Mullins, D. R. Reaction of Formic Acid over Amorphous Manganese Oxide Catalytic Systems: An in Situ Study. *J. Phys. Chem. C* **2010**, *114*, 20000−20006.

(27) Wang, R. H.; Li, J. H. Effects of Precursor and Sulfation on Oms-2 Catalyst for Oxidation of Ethanol and Acetaldehyde at Low Temperatures. *Environ. Sci. Technol.* **2010**, *44*, 4282−4287.

(28) Pahalagedara, L. R.; Dharmarathna, S.; King'ondu, C. K.; Pahalagedara, M. N.; Meng, Y. T.; Kuo, C. H.; Suib, S. L. Microwave-Assisted Hydrothermal Synthesis of A-Mno_2: Lattice Expansion Via Rapid Temperature Ramping and Framework Substitution. *J. Phys. Chem. C* **2014**, *118*, 20363−20373.

(29) Nyutu, E. K.; Chen, C.-H.; Sithambaram, S.; Crisostomo, V. M. B.; Suib, S. L. Systematic Control of Particle Size in Rapid Open-Vessel Microwave Synthesis of K-Oms-2 Nanofibers. *J. Phys. Chem. C* **2008**, *112*, 6786−6793.

(30) Huang, H.; Meng, Y.; Labonte, A.; Dobley, A.; Suib, S. L. Large-Scale Synthesis of Silver Manganese Oxide Nanofibers and Their Oxygen Reduction Properties. *J. Phys. Chem. C* **2013**, *117*, 25352−25359.

(31) Iyer, A.; Del-Pilar, J.; King'ondu, C. K.; Kissel, E.; Garces, H. F.; Huang, H.; El-Sawy, A. M.; Dutta, P. K.; Suib, S. L. Water Oxidation Catalysis Using Amorphous Manganese Oxides, Octahedral Molecular Sieves (Oms-2), and Octahedral Layered (Ol-1) Manganese Oxide Structures. *J. Phys. Chem. C* **2012**, *116*, 6474−6483.

(32) Hou, J. T.; Liu, L. L.; Li, Y. Z.; Mao, M. Y.; Lv, H. Q.; Zhao, X. J. Tuning the K+ Concentration in the Tunnel of Oms-2 Nanorods Leads to a Significant Enhancement of the Catalytic Activity for Benzene Oxidation. *Environ. Sci. Technol.* **2013**, *47*, 13730−13736.

(33) Genuino, H. C.; Dharmarathna, S.; Njagi, E. C.; Mei, M. C.; Suib, S. L. Gas-Phase Total Oxidation of Benzene, Toluene, Ethylbenzene, and Xylenes Using Shape-Selective Manganese Oxide

DOI: 10.1021/acs.jpcc.5b08095
J. Phys. Chem. C 2015, 119, 23119−23126

and Copper Manganese Oxide Catalysts. *J. Phys. Chem. C* **2012**, *116*, 12066−12078.
(34) Hu, B.; Chen, C.-h.; Frueh, S. J.; Jin, L.; Joesten, R.; Suib, S. L. Removal of Aqueous Phenol by Adsorption and Oxidation with Doped Hydrophobic Cryptomelane-Type Manganese Oxide (K−Oms-2) Nanofibers. *J. Phys. Chem. C* **2010**, *114*, 9835−9844.
(35) Opembe, N. N.; King'ondu, C. K.; Espinal, A. E.; Chen, C.-H.; Nyutu, E. K.; Crisostomo, V. M.; Suib, S. L. Microwave-Assisted Synthesis of Manganese Oxide Octahedral Molecular Sieve (Oms-2) Nanomaterials under Continuous Flow Conditions. *J. Phys. Chem. C* **2010**, *114*, 14417−14426.
(36) Li, J. H.; Wang, R. H.; Hao, J. M. Role of Lattice Oxygen and Lewis Acid on Ethanol Oxidation over Oms-2 Catalyst. *J. Phys. Chem. C* **2010**, *114*, 10544−10550.
(37) Peluso, M. A.; Gambaro, L. A.; Pronsato, E.; Gazzoli, D.; Thomas, H. J.; Sambeth, J. E. Synthesis and Catalytic Activity of Manganese Dioxide (Type Oms-2) for the Abatement of Oxygenated Vocs. *Catal. Today* **2008**, *133−135*, 487−492.
(38) Luo, J.; Zhang, Q. H.; Garcia-Martinez, J.; Suib, S. L. Adsorptive and Acidic Properties, Reversible Lattice Oxygen Evolution, and Catalytic Mechanism of Cryptomelane-Type Manganese Oxides as Oxidation Catalysts. *J. Am. Chem. Soc.* **2008**, *130*, 3198−3207.
(39) Luo, J.; Zhang, Q. H.; Huang, A.; Suib, S. L. Total Oxidation of Volatile Organic Compounds with Hydrophobic Cryptomelane-Type Octahedral Molecular Sieves. *Microporous Mesoporous Mater.* **2000**, *35−36*, 209−217.
(40) Yamaguchi, K.; Kobayashi, H.; Wang, Y.; Oishi, T.; Ogasawara, Y.; Mizuno, N. Green Oxidative Synthesis of Primary Amides from Primary Alcohols or Aldehydes Catalyzed by a Cryptomelane-Type Manganese Oxide-Based Octahedral Molecular Sieve, Oms-2. *Catal. Sci. Technol.* **2013**, *3*, 318−327.
(41) Wu, M. C.; Kelly, N. A. Clean-Air Catalyst System for on-Road Applications: Ii. Mechanistic Studies of Pollutant Removal. *Appl. Catal., B* **1998**, *18*, 93−104.
(42) Villegas, J. C.; Garces, L. J.; Gomez, S.; Durand, J. P.; Suib, S. L. Particle Size Control of Cryptomelane Nanomaterials by Use of H_2o_2 in Acidic Conditions. *Chem. Mater.* **2005**, *17*, 1910−1918.
(43) Malinger, K.; Ding, Y.; Sithambaram, S.; Espinal, L.; Gomez, S.; Suib, S. Microwave Frequency Effects on Synthesis of Cryptomelane-Type Manganese Oxide and Catalytic Activity of Cryptomelane Precursor. *J. Catal.* **2006**, *239*, 290−298.
(44) Polverejan, M.; Villegas, J. C.; Suib, S. L. Higher Valency Ion Substitution into the Manganese Oxide Framework. *J. Am. Chem. Soc.* **2004**, *126*, 7774−7775.
(45) Wang, R. H.; Li, J. H. Oms-2 Catalysts for Formaldehyde Oxidation: Effects of Ce and Pt on Structure and Performance of the Catalysts. *Catal. Lett.* **2009**, *131*, 500−505.
(46) Hou, J. T.; Li, Y. Z.; Liu, L. L.; Ren, L.; Zhao, X. J. Effect of Giant Oxygen Vacancy Defects on the Catalytic Oxidation of Oms-2 Nanorods. *J. Mater. Chem. A* **2013**, *1*, 6736.
(47) Wang, Y. F.; Zhang, C. B.; Liu, F. D.; He, H. Well-Dispersed Palladium Supported on Ordered Mesoporous Co_3o_4 for Catalytic Oxidation of O-Xylene. *Appl. Catal., B* **2013**, *142−143*, 72−79.
(48) Rezaei, E.; Soltan, J.; Chen, N. Catalytic Oxidation of Toluene by Ozone over Alumina Supported Manganese Oxides: Effect of Catalyst Loading. *Appl. Catal., B* **2013**, *136−137*, 239−247.
(49) Tang, Q. H.; Huang, X. N.; Wu, C. M.; Zhao, P. Z.; Chen, Y. T.; Yang, Y. H. Structure and Catalytic Properties of K-Doped Manganese Oxide Supported on Alumina. *J. Mol. Catal. A: Chem.* **2009**, *306*, 48−53.
(50) Liu, F. D.; Shan, W. P.; Lian, Z. H.; Xie, L. J.; Yang, W. W.; He, H. Novel $Mnwo_x$ Catalyst with Remarkable Performance for Low Temperature Nh_3-Scr of No_x. *Catal. Sci. Technol.* **2013**, *3*, 2699.
(51) Yang, Y.; Zhang, S. Z.; Wang, S. W.; Zhang, K. L.; Wang, H. Z.; Huang, J.; Deng, S. B.; Wang, B.; Wang, Y. J.; Yu, G. Ball Milling Synthesized Mno_x as Highly Active Catalyst for Gaseous Pops Removal: Significance of Mechanochemically Induced Oxygen Vacancies. *Environ. Sci. Technol.* **2015**, *49*, 4473−4480.
(52) Tang, W. X.; Wu, X. F.; Li, S. D.; Li, W. H.; Chen, Y. F. Porous Mn−Co Mixed Oxide Nanorod as a Novel Catalyst with Enhanced Catalytic Activity for Removal of Vocs. *Catal. Commun.* **2014**, *56*, 134−138.
(53) Li, W.; Gibbs, G. V.; Oyama, S. T. Mechanism of Ozone Decomposition on a Manganese Oxide Catalyst. 1. In Situ Raman Spectroscopy and Ab Initio Molecular Orbital Calculations. *J. Am. Chem. Soc.* **1998**, *120*, 9041−9046.
(54) Sun, H.; Chen, S.; Wang, P.; Quan, X. Catalytic Oxidation of Toluene over Manganese Oxide Octahedral Molecular Sieves (Oms-2) Synthesized by Different Methods. *Chem. Eng. J.* **2011**, *178*, 191−196.
(55) Liu, Y.; Li, X. S.; Liu, J. L.; Shi, C.; Zhu, A. M. Ozone Catalytic Oxidation of Benzene over Agmn/Hzsm-5 Catalysts at Room Temperature: Effects of Mn Loading and Water Content. *Chin. J. Catal.* **2014**, *35*, 1465−1474.

DOI: 10.1021/acs.jpcc.5b08095
J. Phys. Chem. C 2015, 119, 23119−23126